PHYSICAL REVIEW B **94**, 024304 (2016)

Acoustic transmission through compound subwavelength slit arrays

G. P. Ward, A. P. Hibbins, and J. R. Sambles
Electromagnetic and Acoustic Materials Group, Department of Physics and Astronomy, University of Exeter, Stocker Road, Devon EX4 4QL, United Kingdom

J. D. Smith
DSTL, Porton Down, Salisbury, Wiltshire SP4 0JQ, United Kingdom

(Received 16 March 2016; revised manuscript received 1 June 2016; published 12 July 2016)

The angular dependence of the transmission of sound in air through four types of two-dimensional slit arrays formed of aluminium slats is explored, both experimentally and numerically. For a simple, subwavelength periodic slit array, it is well known that Fabry-Perot-like waveguide resonances, supported by the slit cavities, coupled to diffracted evanescent waves, result in enhanced acoustic transmission at frequencies determined by the length, width, and separation of each slit cavity. We demonstrate that altering the spacing or width of some of the slits to form a compound array (i.e., an array having a basis comprised of more than one slit) results in sharp dips in the transmission spectra, which may have a strong angular dependence. These features correspond to phase resonances, which have been studied extensively in the electromagnetic case. This geometry allows for additional near-field configurations compared to the simple array, whereby the field in adjacent cavities can be out of phase. Several types of compound slit arrays are investigated; one such structure is optimized to minimize the effect of boundary-layer loss mechanisms present in each slit cavity, thereby achieving a deep, sharp transmission minimum in a broad maximum.

DOI: 10.1103/PhysRevB.94.024304

The experimental discovery of extraordinary optical transmission (EOT) through subwavelength hole arrays [1] opened a new area of research into how structured resonant layers can affect the propagation of light. This research has been extended to the acoustic case, where similar behavior is observed, sometimes termed enhanced acoustic transmission (EAT) (not extraordinary, since longitudinal sound waves have no cutoff when propagating through gaps/holes in rigid bodies with sound-hard walls) [2–7]. The observed phenomena for both electromagnetic and acoustic cases in such structures is due to the complex interplay between surface-wave (or surface-wave-like) modes and waveguide modes, the exact nature being dependent on many structural parameters [6–8]. Other types of transmission anomalies have been discovered in the electromagnetic case that stem from EOT. One such anomaly is the phase resonance, which appears as a sharp dip in the transmission of transverse magnetic polarized light through so-called compound grating structures, i.e., gratings with structure factor comprised of multiple elements [9–14]. In the case of a two-dimensional (2D) metal slit array, this can be achieved by having unequally sized slits or multiple slits in each period. In a singularly periodic grating structure, symmetry requires that the fields in all slit cavities are identical when excited by a normally incident planar wave. Compound gratings introduce new degrees of freedom to the near-field configurations and, at specific frequencies, fields in adjacent cavities may be both out of phase with one another and strongly enhanced [10], leading to phase-resonant features in their electromagnetic response. Being simply a lattice/symmetry phenomena, there is an expectation that these phase resonances will also exist in the acoustic case [15–17].

Here, we experimentally demonstrate the existence of the airborne acoustic phase resonance with a compound slit-array grating, finding good agreement with numerical model predictions. We also optimize the grating structure to achieve the strongest possible coupling to the phase resonance, with viscous and thermal boundary layer effects being accounted for.

The experimental samples are illustrated in Fig. 1 and the measurement setup is illustrated in Fig. 2. J denotes the number of slits per grating period, with $J = 3$a and $J = 3$b having the same number of slits but with different slit-width ratios. Such gratings are formed of aluminium slats of size $600 \times 2.9 \times 19.8$ mm, stacked in a wooden sample holder, with small polyester spacers used to create the appropriately sized air gaps. The total sample area is 560×400 mm, and it is placed with the slats vertical, on a rotating table, symmetrically situated between two spherical mirrors 3 m apart, of radius 220 mm and focal length 1 m. One mirror collimates the sound of a speaker placed at its focal point, directed so that the beam is normal to the face of the slit cavities when the rotating table is set to $\theta = 0^\circ$ (normal incidence) producing a beam width smaller than the sample face to approximate an infinite sample size. The other mirror focuses the beam transmitted through the sample onto a Brüel and Kjær 4190 microphone. The speaker is driven by a signal generator producing a Gaussian pulse centered on 8 kHz, containing a broad range of audible frequencies. The sample is rotated between $-2.5^\circ \leqslant \theta \leqslant 65^\circ$ (limited by the sample size and frame), and the averaged time-domain signal from multiple pulses of the speaker for each angle is recorded by a PC-based oscilloscope. To account for small leakage of the signal around the sample, a large sound opaque slab with antireflection absorber foam attached is placed on the incident side of the source. Transmission measurements are then repeated for all angles, and the resulting data are subtracted from the original sample data in the time-domain spectra, leaving only the signal transmitted through the sample holder. This is then Fourier analyzed to obtain the angular-dependent frequency response of the sample. A reference spectrum for each angle is obtained

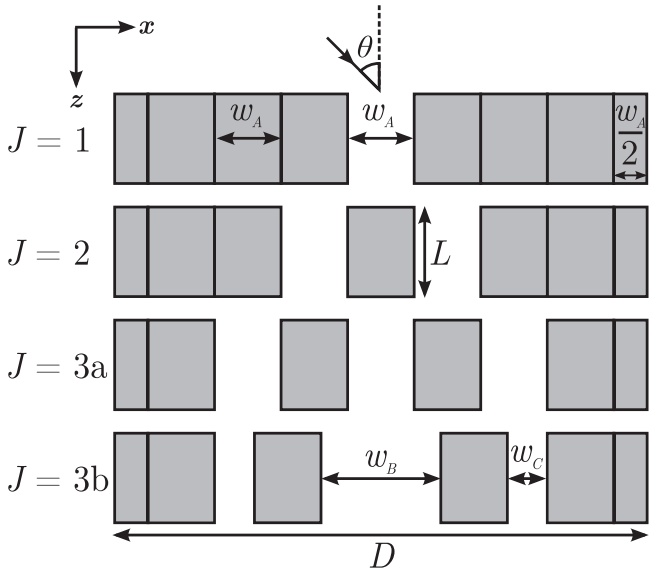

FIG. 1. Schematic of a unit cell of each array sample (not to scale). The gray blocks represent the aluminium slats that form the sample, of width $w_A = 2.9$ mm and length $L = 19.8$ mm. The air gaps that form the cavities are the same size as the slats, except for the $J = 3$b sample, where the central cavity w_B has width 5.9 mm, and the outer two have $w_C = 1.5$ mm. Each sample has a period $D = 8w_A = 23.2$ mm.

by repeating the experiment with only the wooden sample frame in place, and used to normalize the transmitted signal in the frequency domain.

Figure 3 shows the transmissivity spectra for each sample when probed at normal incidence, as a function of the ratio of array periodicity D to incident wavelength of radiation λ. Also included are the predicted spectra calculated using a finite-element method (FEM). The red dashed line is the result obtained from the model solving the lossless acoustic wave equation, while the blue long-dashed line comes from a model which solves the linearized Navier-Stokes equation,

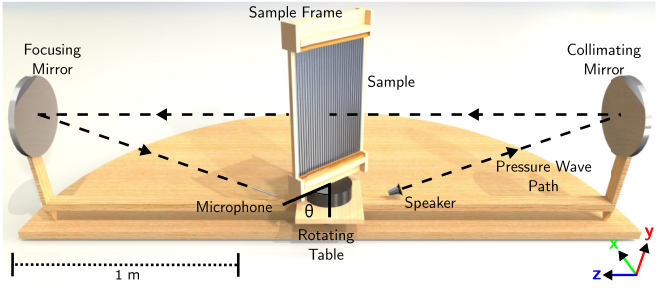

FIG. 2. To-scale schematic of the transmission measurement experimental setup, labeled accordingly. The speaker was placed at the focal point of the first mirror, which directed the collimated beam toward the sample. The transmitted signal was then focused onto the microphone by the second mirror. The sample frame was placed onto a computer controlled rotating table, allowing control of the incident angle θ. An acoustic absorber was placed at appropriate positions to reduce unwanted reflections from the solid surfaces that make up the measuring kit (not shown).

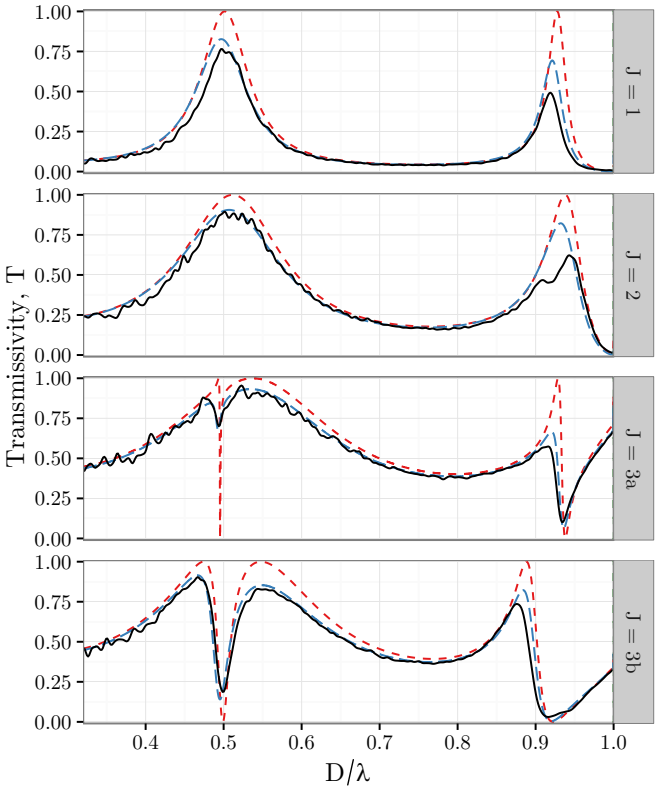

FIG. 3. Normal-incidence transmissivity spectra as a function of the ratio of array periodicity D to incident radiation wavelength λ for each of the sample types illustrated in Fig. 1. The solid black line is the experimental data, the short-dashed red and long-dashed blue lines are the lossless and viscous-thermal loss-including numerical model spectra for comparison. The diffraction edge for each experimental sample occurs when $\frac{D}{\lambda} = 1$. Fluctuations in the ambient temperature are accounted for in the calculation of λ.

accounting for viscous and thermal boundary layer effects at each rigid, sound-hard wall [18]. The position of the onset of diffraction corresponds to $\frac{D}{\lambda} = 1$. The calculated incident wavelength for each sample takes into account changes in ambient temperature between measurements, acting to vary the speed of sound in air c. Atmospheric pressure and humidity changes have a negligible effect [19].

It is well known that sound incident on an air cavity bounded by two parallel, infinitely wide, rigid-solid walls of length L will have a broad transmission peak at a frequency naïvely predicted by the Fabry-Perot condition, $f_{\mathrm{FP}} = \frac{nc}{2L}$, where c is the speed of sound and n is an integer. There is a correction ΔL that takes into account end effects at the exit/entrance of each cavity, which to first order is approximated by $\Delta L = \frac{8w}{3\pi}$, with w being the width of the slit [20]. When such cavities are placed in an equally spaced array of period D, such as in sample $J = 1$, the coherent effect of these diffractive evanescent waves is to form a collective resonance, which is guided along the surface of the grating but decays exponentially away from it [21]. Thus, in the air, they are surface-wave-like in character and are henceforth referred to as spoof-surface-acoustic waves (SSAWs). The enhanced fields associated with the SSAW on each face of the array couple together via the FP-like modes in the slit cavities. This is the mechanism by which EAT can

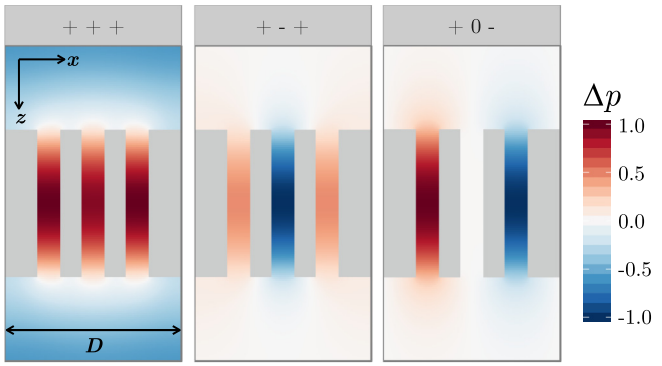

FIG. 4. FEM simulations of the instantaneous pressure fields Δp corresponding to the three available eigenmodes, $+++$, $+-+$, and $+0-$, of the $J = 3$a system when there is no net phase shift along x between unit cells, shown at a temporal phase corresponding to maximum field amplitude. The color scales have been normalized with normalization constants 2.19, 4.01, and 3.39, respectively. The three eigenmodes have resonant frequencies which correspond to $\frac{D}{\lambda}$ values of 0.54, 0.5, and 0.48, respectively. These were calculated using a loss-free FEM model. The gray blocks represent the aluminium slats, in the same orientation as illustrated in Fig. 1.

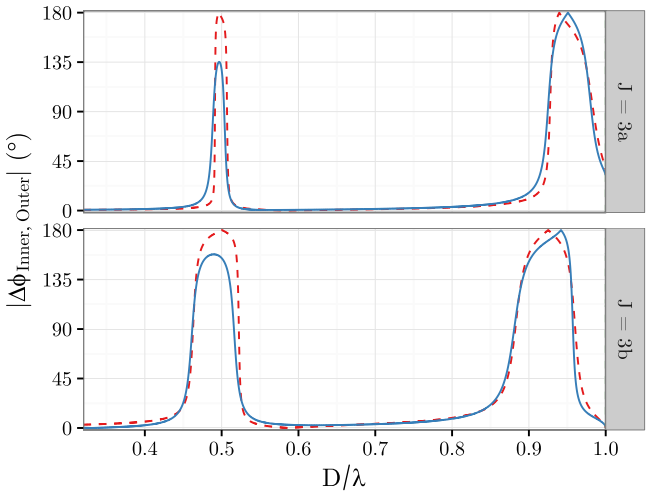

FIG. 5. Lossless (dotted red line) and viscous-thermal (solid blue line) FEM models of the difference in the phase $|\Delta\phi_{\text{Inner, Outer}}|$ of the tangential particle velocity V_x of the central and outer cavities, for the $J = 3$a and $J = 3$b samples, plotted as a function of the ratio of array periodicity to incident wavelength $\frac{D}{\lambda}$. The predicted diffraction edge is at $\frac{D}{\lambda} = 1$. Phases were evaluated in the center of each cavity on the transmitting side of the grating.

occur at specific frequencies, resulting in large peaks in the transmission spectrum of such a grating. Indeed, Fig. 3 shows two broad peaks in the $J = 1$ spectrum, at $\frac{D}{\lambda} = 0.5$ and 0.92. These correspond to the first- and second-order FP-like modes, with the frequency of the $n = 2$ mode perturbed by the strong evanescent diffracted fields near the onset of diffraction. This mechanism has been studied extensively in the past decade [4–7].

The transmission spectrum of the $J = 2$ sample is little different, except for a slight broadening of the FP modes and a small upward frequency shift due to a reduction in the strength of the Fourier amplitude component of the grating profile that causes first-order scattering. For the $J = 3$ samples as well as further broadening of the FP-like modes, a new feature, i.e., the phase resonance, appears in the low-frequency wing of each primary resonance. As described in the electromagnetic case by both Skigin *et al.* [10] and Hibbins *et al.* [12], this is because there is a new degree of freedom in the system. In the $J = 1$ and $J = 2$ cases, the fields in each adjacent cavity must have identical phase at normal incidence; hence an incident planar wave cannot excite a phase resonance. However, with three cavities per period, the outer two slits have different surroundings to the central one. Hence, by symmetry, two field configurations can now be excited at normal incidence: all of the fields in phase (labeled the $+++$ mode), and the central and outer cavity fields out of phase (the $+-+$ mode, where $-$ corresponds to a phase shift of π relative to $+$). This is illustrated in both Figs. 4 and 5.

Figure 4 shows the instantaneous pressure field of the eigenmodes of the $J = 3$a system with no net phase change across the unit cell in the x direction (which simulates excitation by a plane wave at normal incidence), calculated with the lossless FEM model, and normalized to their maximum amplitude of Δp, different for each mode. The mode labeled $+++$ corresponds to the primary resonance at $\frac{D}{\lambda} = 0.53$, where all of the cavities are resonating in phase, with similar amplitude. This mode is highly radiative and results in the broad transmission peak, with the maximum absolute pressure amplitude within the slits being 3.1 greater than in the incident wave. The second panel of Fig. 4, with the mode labeled $+-+$, illustrates the phase-resonance eigenmode that is excitable at normal incidence. The outer two cavities are oscillating exactly π out of phase with the central one, which, as the color scale shows, has a greater field amplitude. Note that the maximum absolute pressure field amplitude within the cavities has now become 55.7 times greater than in the incident wave, a significant increase compared to the $+++$ mode, indicating a stronger degree of localization. Another interesting feature is the apparent standing wave that has formed across the x direction, seen from looking at just the top or bottom of the slits—the cavity resonances appear to be coupled with each other. There is a third field configuration available in the form of the antisymmetric $+0-$ mode, where the outer two cavities are π radians out of phase with each other, and $\pi/2$ radians out of phase with the central cavity, having no mode amplitude. The $J = 2$ configuration supports a similar $+-$ mode, but in neither configuration are these modes excitable by an incoming plane wave at normal incidence, as they require a phase change along the surface (incidentally, a weak feature has appeared in the experimental data for the $J = 2$ sample as the collimating mirror does not produce a perfect planar wave, and allows weak coupling to this mode). Direct coupling to any of the phase-resonant configurations is impossible as the pressure field within the slit cavities is out of phase with the incident field. Hence, they can only be excited via coupling between slits, and appear as sharp dips in transmission, sat in the primary $+++$ resonance peak.

Another way of illustrating the phase resonance is shown in Fig. 5, which is a plot of the numerically calculated phase difference $|\Delta\phi_{\text{Inner, Outer}}|$ of the velocity field V_x between

the central and outer slits, evaluated at the midwidth of the transmitting side of each slit cavity. The structure was excited by a normally incident planar wave, with varying frequency. For both $J = 3$a and $J = 3$b samples, at frequencies corresponding to the position of the transmission dips in Fig. 3, the lossless acoustic-wave equation model (red dashed line) predicts a π phase difference between the slits, while away from these resonances and below the onset of diffraction, $|\Delta\phi_{\text{Inner, Outer}}|$ is close to zero.

To obtain the strongest possible reduction in transmission at the phase-resonant frequency, there must be a perfect balance between the radiative and nonradiative losses in the system. This is the well-known critical coupling condition. Nonradiative thermodynamic loss effects form a part of this balance and thus must be accounted for. With sample $J = 3$a, the $+-+$ resonance is a weak feature in the experiment, only reducing transmission by 15% at $\frac{D}{\lambda} = 0.49$, being much stronger in the second-order mode ($\frac{D}{\lambda} = 0.94$), reaching a reduction of ~50%. The lossless FEM model, solving the acoustic-wave equation, predicts a very sharp, 100% deep resonance at $\frac{D}{\lambda} = 0.49$ in the transmission spectrum. However, when viscous-thermal contributions are included (via solving of the linearized Navier-Stokes equation)—which results in a much better agreement with the experimental data—this resonance is significantly more damped. The effect stems from the viscous-thermal boundary layers at the rigid, sound-hard walls that cause significant attenuation of the fields within the slit cavities [18]. Note that we have checked that a simpler model that includes only a bulk loss term added to the free-space acoustic-wave equation does not predict the increased damping effect.

Sample $J = 3$b is optimized geometrically to balance the radiative and nonradiative loss effects as close to critical coupling as possible while keeping periodicity and slat size constant. This grating is a simple modification of the $J = 3$a sample, with an inner-cavity-to-outer-cavity ratio of around four to one. As Fig. 3 shows, the experimental data exhibits a much deeper, broader phase resonance in both the fundamental and second-order modes. Figure 5 gives extra insight into this phenomenon, showing that the loss-inclusive model for the $J = 3$a sample predicts a maximum $|\Delta\phi_{\text{Inner, Outer}}|$ of $\sim 0.75\pi$ radians at the occurrence of the phase resonance, while it reaches $\sim 0.9\pi$ radians for the optimized $J = 3$b sample, thus displaying stronger coupling to the $+-+$ eigenmode.

By recording angle (θ) dependent data, we map the dispersion and attain a greater understanding of the origin of these modes. Figure 6 shows the transmissivity of each grating as a function of the ratio of array periodicity to incident wavelength, and reduced in-plane wave vector $\frac{k_x}{k_g}$, where $k_x = k_0 \sin\theta$ and $k_g = \frac{2\pi}{D}$.

The sample $J = 1$ grating exhibits a fundamental mode that is largely flat banded, being strongly localized in the slit cavity with FP-like fields, where the cavity's length L and width w_A are the dominant variables in determining the resonance position. This mode starts from the FP frequency at $k_x = 0$, and only becomes perturbed as the diffracted sound line from $k_x = k_g$ is approached. There is similar to the perturbation of the second-order mode ($\frac{D}{\lambda} = 0.9$).

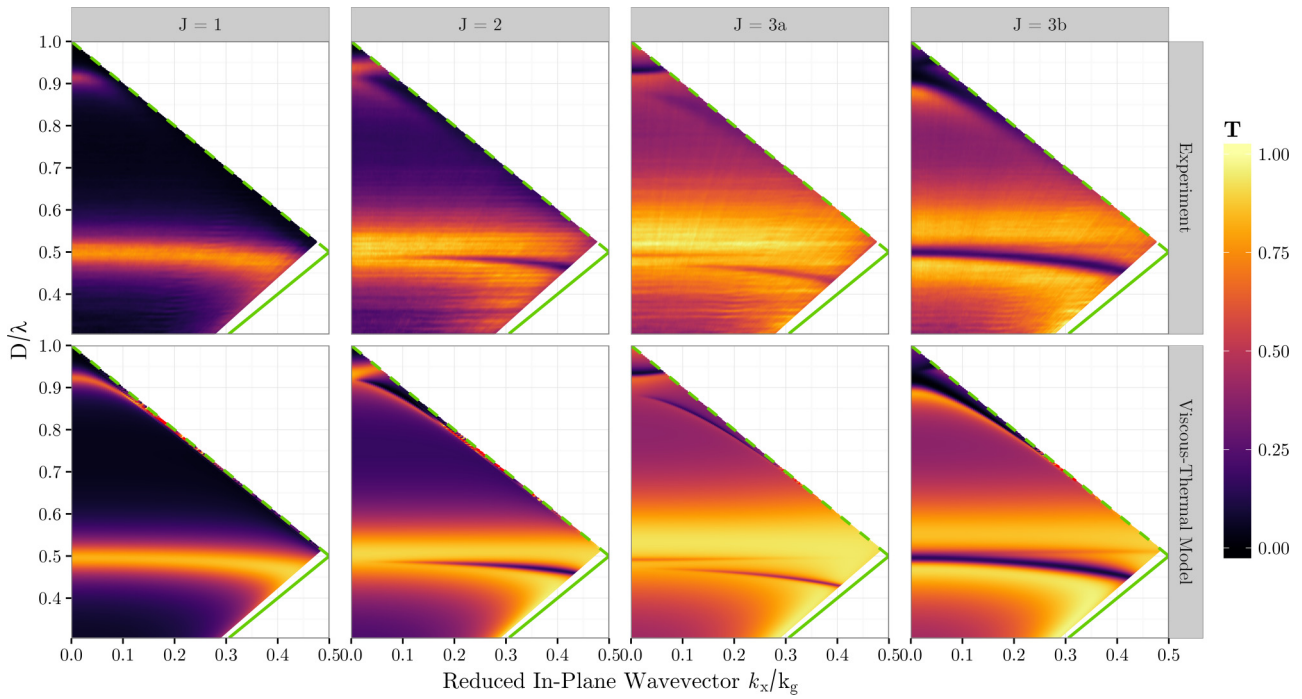

FIG. 6. Transmission data illustrating mode dispersion for each sample illustrated in Fig. 1, labeled accordingly. The ratio of array periodicity to incident wavelength $\frac{D}{\lambda}$ is plotted as a function of reduced in-plane wave vector $\frac{k_x}{k_g}$, where a value of $\frac{k_x}{k_g} = 0.5$ corresponds to the first Brillouin-zone boundary. The top row is the recorded experimental data, whereas the bottom row is the numerical results calculated by the viscous-thermal loss-inclusive FEM model. For reference, a solid green line representing grazing incidence k_0 is included on each plot. The onset of first-order diffraction is represented by the green dashed line. Fluctuations in ambient room temperature are accounted for in all calculations of λ.

Additional transmission dips become apparent in the response of the $J = 2$,3a, and 3b samples at $\frac{D}{\lambda} = 0.5$ and $0.1 \leqslant \frac{k_x}{k_g} \leqslant 0.4$. These are the antisymmetric phase resonances that can now be excited with the addition of a phase difference along the grating surface [11,12], associated with $\theta \neq 0$. For $J = 2$, at high k_x, it is now possible to excite the $+ -$ mode, where the two cavities are π radians out of phase. The $J = 3$a and $J = 3$b samples also exhibit the additional feature, which has appeared on the low-frequency wing of the FP resonance at $\frac{D}{\lambda} = 0.5$. This corresponds to the antisymmetric $+ 0 -$ phase resonance shown in Fig. 4. In all cases, one can see that at least one of the phase resonances has a strong k_x dependence, indicating that they are surface-wave-like in character. It is possible to deploy a surface-wave band-folding picture to explain the dispersion relations in Fig. 6. To understand this, it is helpful to plot the band structure of each sample using the extended zone scheme representation, i.e., by drawing the band structure without band folding present. This is illustrated in Fig. 7.

Adding structure factor to each grating periodicity opens up new degrees of freedom to the system, and allows coupling of the phase-resonant near-field configurations to diffracted fields (SSAWs) that originate from the diffractive end effects. Figure 7 is a plot of the underlying band structure of the eigenmodes of the $J = 1$, $J = 2$, and $J = 3$a samples, in the form of a dispersion diagram with the same axes as those in Fig. 6. The eigenfrequencies were calculated using the loss-free FEM model.

With one cavity per unit cell, the $J = 1$ configuration has only two modes available (considering only first-order harmonics): the naturally radiative primary FP-like resonance (denoted by the solid blue line) and the low-frequency SSAW (denoted by the solid orange line) that is only accessible in the nonradiative regime as it has in-plane wave vector $k_x > k_0$. Here, k_0 is represented by the black dashed line, i.e., the sound line. This is the wave vector that a grazing incidence pressure wave would possess. Since this structure only has one cavity per unit cell, and the sample walls can be treated as perfectly rigid, the only degree of freedom available to the near field is the cavity being either a positive or negative antinode. This means that any mode which has a shorter surface wavelength than the spacing of the cavities D *cannot* exist, as they must require a pressure field maximum within the rigid walls. Thus, beyond the first Brillouin zone at $k_x = \frac{k_g}{2}$, the SSAW ceases to exist—at normal incidence, with band folding (where the grating periodicity k_g can be added or subtracted to any mode, thereby scattering nonradiative modes into the radiative regime), we will only see the primary FP-like mode.

When there are two cavities per unit cell (sample $J = 2$), there is another possible field configuration apart from the FP-like $++$ mode. The adjacent cavities can now oscillate π radians out of phase with each other, creating the antisymmetric $+ -$ phase resonance. Now, it is possible for a SSAW with a shorter wavelength than D to exist, since the extra antinode per unit cell it requires can now be satisfied. Thus, the low-frequency SSAW which previously vanished above $k_x = \frac{k_g}{2}$ now band splits at this first Brillouin zone, and continues up to the next one at $k_x = k_g$. This mode is represented by the green line in Fig. 7, and is band folded

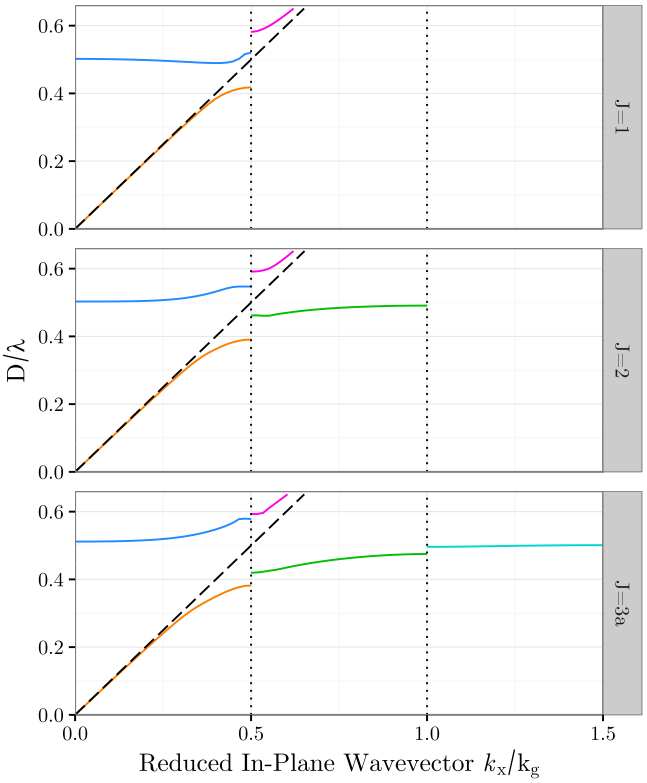

FIG. 7. Dispersion diagrams showing the extended zone scheme representation of the eigenmodes of the $J = 1$, $J = 2$, and $J = 3$a systems (all labeled), plotted as a function of the ratio of array periodicity to incident wavelength $\frac{D}{\lambda}$ vs reduced in-plane wave vector $\frac{k_x}{k_g}$. Individual eigenfrequencies were calculated using loss-free FEM models. The sound line k_0 is represented by the black dashed line. Integer and half-integer values of $\frac{k_x}{k_g}$ correspond to different Brillouin-zone boundaries, which have been marked with vertical black dotted lines. The solid lines represent the different eigenmodes supported by each grating structure, with colors signifying different field configurations. Blue is the naturally radiative Fabry-Perot-like mode, with pink being its band split pair. Orange is the nonradiative low-frequency SSAW, green is the SSAW coupled to the low-energy phase resonance, and cyan is the SSAW coupled to the high-energy phase resonance.

back into the radiative regime by first-order scattering from k_g, forming the deep, sharp resonance in our experimental data for the $J = 2$ sample at high k_x. Above $k_x = k_g$, the SSAW again ceases to exist; as before, it requires another antinode per unit cell, and this is forbidden by the lack of a possible near-field configuration.

Finally, by increasing the number of cavities per unit cell to three (sample $J = 3$a), yet another degree of freedom is available to the near field. There is now the primary $+++$ configuration, the $+ - + \pi$ mode, and the $+0-$ antisymmetric mode. Thus, the three-antinodes-per-unit-cell condition required for wave vectors larger than $k_x = k_g$ is satisfied, the SSAW band splits at $k_x = k_g$ and extends to the next Brillouin zone at $k_x = \frac{3k_g}{2}$, where the same pattern repeats, and beyond this the mode ceases to exist. The second-order scattering at $k_x = 2k_g$ band folds this SSAW back into the radiative regime, resulting in the two sharp

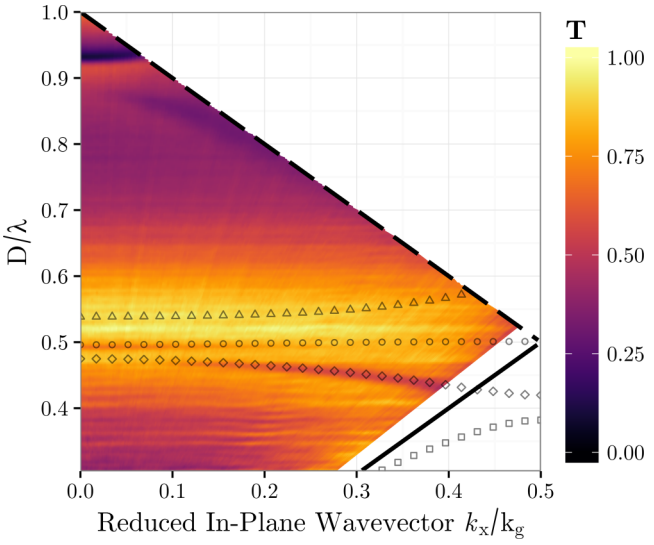

FIG. 8. Dispersion diagram showing the experimental transmissivity T data for the $J = 3$a sample, with its numerically calculated eigenfrequencies overlaid, plotted as a function of the ratio of array periodicity to incident wavelength $\frac{D}{\lambda}$ vs reduced in-plane wave vector $\frac{k_x}{k_g}$. The value of $\frac{k_x}{k_g} = 0.5$ corresponds to the first Brillouin-zone boundary. The solid black line represents the wave vector k_0 of a grazing incidence pressure wave. The onset of first-order diffraction is represented by the black dashed line, being $\frac{D}{\lambda} = 1$ at normal incidence ($\frac{k_x}{k_g} = 0$). The hollow points represent the different eigenmodes supported by the $J = 3$a grating structure, with shapes signifying different field configurations. The triangles are the naturally radiative Fabry-Perot-like mode, circles are the SSAW coupled to the $+-+$ phase resonance, and the diamonds are the SSAW coupled to the $+0-$ phase resonance. The squares are the nonradiative low-frequency SSAW which cannot be seen in this transmission experiment.

dips seen in the experimental dispersion data for the $J = 3$a sample (the band structure for the $J = 3$b sample is identical in shape since it has the same number of cavities per unit cell; only the coupling strengths and frequencies have changed). This is illustrated in Fig. 8, where the band-folded eigenmodes calculated using the loss-free FEM model are overlaid onto the $J = 3$a experimental transmission data. One can see that the dips in transmissivity correspond to the diffracted SSAWs. Using this band-folding picture, it is easy to see that every time one adds an air cavity to the unit cell, a new degree of freedom is available to the near field, and hence a shorter wavelength SSAW is able to be band folded back into the radiative regime, resulting in the appearance of a sharp dip in the transmission spectrum.

It is important to note that the frequency ordering of the modes' field configuration is not fixed at normal incidence. This is demonstrated by a further change in behavior visible between the $J = 3$a and $J = 3$b samples in Fig. 6. For the identical width cavity $J = 3$a case, one can see that the $+0-$ mode that is not excitable at normal incidence is occupied by the low-energy band with high curvature, while the $+-+$ configuration is coupled to the high-energy flat-banded mode. When the central slit is widened to create the $J = 3$b sample, this behavior is reversed, and now the low-energy band is excitable at normal incidence. This is because widening the central cavity has redistributed the energies of the SSAWs coupling to the $+-+$ configuration and the $+0-$ configuration, where the $+0-$ SSAW now has the greater energy of the two (possessing a sharper field gradient) and is at a higher frequency. This highlights an important point. At arbitrary values of k_x, it is meaningless to assign $+0-$ and $+-+$ labels to each of the modes, as there is no standing wave formed across the grating surface. This is only true when k_x is some integer value of k_g, and hence the surface mode phase change is commensurate with the grating periodicity. In addition, such a labeling system still breaks down at the first Brillouin zone $k_x = \frac{k_g}{2}$; the π phase shift across each unit cell in the x direction requires that two be labeled before the pattern repeats. This results in, for example, the $+-+-+-$ or $+0\ -\ -0+$ configurations. Incidentally, the order of the field configurations at normal incidence bears no relation to how they appear at this first Brillouin zone. If at normal incidence the mode labeled $+0-$ is at the higher energy, it will evolve to look like the $+-+-+-$ mode at the first Brillouin zone. The former's pressure field is forced through a π phase shift between every cavity, so this field configuration always possesses a greater energy than the $+0\ -\ -0+$ configuration, no matter what the sizes or separations of the cavities are.

A further change in behavior is visible when the central cavity is widened. In the $J = 3$b sample, the $+0-$ mode is significantly weaker than it was for the $J = 3$a configuration. Narrowing the cavities to 1.5 mm has both increased the quality factor of the mode and increased the relative size of the viscous and thermal boundary layers, leading to significant attenuation [18].

We have checked that it is possible to pull the frequency of the primary $+++$ mode down below the $+-+$ and $+0-$ phase resonances by heavily perturbing the grating structure, so that the two inner rigid slats are very thin and thus the three cavities are very closely spaced (with periodicity constant). This increases the coupling strength between cavities, so that they begin to behave as a single wide cavity, thus increasing length correction ΔL, thereby reducing the resonant frequency. This also increases the strength of the first-order scattering Fourier component, again acting to reduce the resonant frequency. The phase resonances are simultaneously pushed to a higher frequency; the phase shift between cavities has to occur over a shorter distance in x, increasing their energy as before.

In conclusion, we have experimentally and numerically demonstrated the existence of the acoustic phase-resonance phenomenon, by studying the transmission of sound through a 2D array of airborne metal slits arranged in four separate configurations. We find that increasing the number of cavity slits per array period, while keeping that period constant, opens up new degrees of freedom to the near field. As well as the standard coupling of the Fabry-Perot modes with diffracted evanescent waves that result in broad transmission peaks, we find dips in the normal-incidence transmission spectra that appear when there are three cavities per grating period, being the phase-resonant modes. We also map out the transmission of these structures as a function of incident angle θ, and find that extra field configurations can be excited with the addition

of a phase change across the grating surface, for any sample that has more than one slit per period. With this information, we describe the origin of each feature with a surface-wave band-folding picture; each mode is a diffractively coupled spoof-acoustic-surface wave, which can be excited via the new field configurations. Finally, we demonstrate the importance of including thermodynamic loss effects when modeling this sort of structure. We optimize one of our samples taking attenuation by viscous and thermal boundary layer effects into account, resulting in measured broad and deep phase resonances that could be useful for the design of acoustic filters.

The authors would like to thank the UK Ministry of Defence's Defence Science and Technology Laboratorty (DSTL) for their financial support and permission to publish.

[1] T. Ebbesen, H. Lezec, H. F. Ghaemi, T. Thio, and P. Wolff, Nature (London) **391**, 667 (1998).
[2] X. Zhang, Phys. Rev. B **71**, 241102 (2005).
[3] L. Zhou and G. A. Kriegsmann, J. Acoust. Soc. Am. **121**, 3288 (2007).
[4] B. Hou, J. Mei, M. Ke, W. Wen, Z. Liu, J. Shi, and P. Sheng, Phys. Rev. B **76**, 054303 (2007).
[5] M. H. Lu, X. K. Liu, L. Feng, J. Li, C. P. Huang, Y. F. Chen, Y. Y. Zhu, S. N. Zhu, and N. B. Ming, Phys. Rev. Lett. **99**, 174301 (2007).
[6] J. Christensen, L. Martin-Moreno, and F. J. Garcia-Vidal, Phys. Rev. Lett. **101**, 014301 (2008).
[7] X. Wang, J. Appl. Phys. **108**, 064903 (2010).
[8] L. Martín-Moreno, F. J. García-Vidal, H. J. Lezec, K. M. Pellerin, T. Thio, J. B. Pendry, and T. W. Ebbesen, Phys. Rev. Lett. **86**, 1114 (2001).
[9] A. N. Fantino, S. I. Grosz, and D. C. Skigin, Phys. Rev. E **64**, 016605 (2001).
[10] D. C. Skigin and R. A. Depine, Phys. Rev. Lett. **95**, 217402 (2005).
[11] D. C. Skigin and R. A. Depine, Phys. Rev. E **74**, 046606 (2006).
[12] A. P. Hibbins, I. R. Hooper, M. J. Lockyear, and J. R. Sambles, Phys. Rev. Lett. **96**, 257402 (2006).
[13] D. C. Skigin, H. Loui, Z. Popovic, and E. F. Kuester, Phys. Rev. E **76**, 016604 (2007).
[14] H. J. Rance, O. K. Hamilton, J. R. Sambles, and A. P. Hibbins, Appl. Phys. Lett. **95**, 041905 (2009).
[15] Z. Liu and G. Jin, J. Phys.: Condens. Matter **21**, 445401 (2009).
[16] H. Estrada, V. Gómez-Lozano, A. Uris, P. Candelas, F. Belmar, and F. Meseguer, J. Phys.: Condens. Matter **23**, 135401 (2011).
[17] H. Zhang, L. Fan, J. Qu, and S. Zhang, J. Appl. Phys. **119**, 084902 (2016).
[18] G. P. Ward, R. K. Lovelock, A. R. J. Murray, A. P. Hibbins, J. R. Sambles, and J. D. Smith, Phys. Rev. Lett. **115**, 044302 (2015).
[19] O. Cramer, J. Acoust. Soc. Am. **93**, 2510 (1993).
[20] L. E. Kinsler, A. R. Frey, A. B. Coppens, and J. V. Sanders, in *Fundamentals of Acoustics*, 4th ed. (Wiley, New York, 1999), Vol. 1, p. 274.
[21] L. Kelders, J. F. Allard, and W. Lauriks, J. Acoust. Soc. Am. **103**, 2730 (1998).